E19-2005-112

E. Tsyganov[1,*], P. Antich[1], P. Kulkarni[1], R. Mason[1], R. Parkey[1],
S. Seliuonine[1], J. Shay[1], T. Soesbe[1], V. Zhezher, A. Zinchenko

COMBINING DIFFERENT MODALITIES
FOR 3D IMAGING OF BIOLOGICAL OBJECTS

---

[1]The University of Texas Southwestern Medical Center, Dallas, USA
*E-mail: Edward.Tsyganov@UTSouthwestern.edu

Цыганов Э. и др.   E19-2005-112
Комбинирование различных методик получения
трехмерных изображений биологических объектов

Однофотонный томограф (микроСПЕКТ) с улучшенным разрешением на NaI(Tl)-сцинтилляторе, использующий точечный коллиматор, был изготовлен и протестирован на небольших животных. Прибор позволяет измерять глубину взаимодействия в толстом кристалле сцинтиллятора с помощью координатно-чувствительного ФЭУ, регистрирующего зависящие от глубины профили сцинтилляционного света. Такое измерение устраняет ошибку параллакса, которая ухудшает высокое пространственное разрешение, требуемое для сканирования небольших животных. Эта новая методика трехмерной регистрации гамма-лучей была применена в микроСПЕКТе и проверена на источнике ^{57}Co и препарате ^{98m}Tc-MDP, введенном в ткани мыши.

Для увеличения исследовательских возможностей томографии ее разновидности могут быть скомбинированы. В частности, как предложено и показано в данной работе, оптическое сканирование может быть использовано для трехмерной реконструкции поверхности кожи животного. Это позволяет улучшить визуализацию и делает возможными поправки на глубину, необходимые для пространственной локализации биолюминесценции в биологических объектах. Такая структурная информация может быть еще более детализирована при использовании рентгеновской томографии, как показано в работе.

Работа выполнена в Лаборатории высоких энергий им. В. И. Векслера и А. М. Балдина ОИЯИ.

Tsyganov E. et al.   E19-2005-112
Combining Different Modalities for 3D Imaging of Biological Objects

A resolution enhanced NaI(Tl)-scintillator micro-SPECT device using pinhole collimator geometry has been built and tested with small animals. This device was constructed based on a depth-of-interaction measurement using a thick scintillator crystal and a position sensitive PMT to measure depth-dependent scintillator light profiles. Such a measurement eliminates the parallax error that degrades the high spatial resolution required for small animal imaging. This novel technique for 3D gamma-ray detection was incorporated into the micro-SPECT device and tested with a ^{57}Co source and ^{98m}Tc-MDP injected in mice body.

To further enhance the investigating power of the tomographic imaging different imaging modalities can be combined. In particular, as proposed and shown in this paper, the optical imaging permits a 3D reconstruction of the animal's skin surface thus improving visualization and making possible depth-dependent corrections, necessary for bioluminescence 3D reconstruction in biological objects. This structural information can provide even more detail if the x-ray tomography is used as presented in the paper.

The investigation has been performed at the Veksler and Baldin Laboratory of High Energies, JINR.

INTRODUCTION

Single Photon Emission Computed Tomography (SPECT) is widely used in clinical and research laboratories. SPECT detects radiolabeled agents at the picomolar level revealing normal and perturbed biochemical and physiological function and provides non-invasive methods to perform in vivo radiopharma-ceutical studies, molecular imaging, gene therapy and to evaluate tumor therapy results. Small animal SPECT devices usually use pinhole collimators to go to sub-millimeter resolution. Good description of the SPECT technique can be found in [1–3].

A common problem with SPECT is the need for anatomical co-registration, so that signals may be associated with organs and tissues. One approach is the addition of x-ray Computed Tomography (CT). Another option of co-registration for a small animal device is optical imaging. Both of these approaches were adopted here.

We have developed a NaI(Tl)-scintillator pinhole-collimated micro-SPECT device featuring a novel technique for 3D position measurement in thick scintil-lators [4–7]. As was previously mentioned, in micro-SPECT the small pinhole size provides the sub-millimeter resolution. However, interaction parallax in the detector could degrade the potential pinhole resolution. To minimize this effect, we have initially used a restricted field of view but are currently developing a detector featuring a depth-of-interaction (DOI) measurement with an extended field of view. The device was built and tested with phantoms and small animals.

Fig. 1. The principle of measuring the Depth of Interaction (DOI) in a blackened crystal. The lower plane of the crystal is attached to a photocathode of a PSPMT. The diameter of the light spot is proportional to the vertical position of an interaction
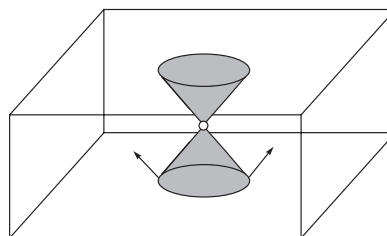
To provide the DOI measurement, a Hamamatsu R2486 Position-Sensitive Photomultiplier Tube (PSPMT) is mounted to the base of the detector crystal. The scintillator crystal is blackened on all sides except the side in contact with

1

the photocathode. This eliminates the light from total internal reflections within the crystal, with the width of the scintillation light profile determining the DOI. The principle of measurements is illustrated in Fig. 1.

Optical imaging has become a powerful tool in biology and medical research. Cooled charge coupled devices (CCD) permit the acquisition of images at very low intensity levels for a wide range wavelengths. Optical imaging is a fast and convenient method of biological interrogation.

A 3D reconstruction algorithm for optical imaging was proposed and tested with animals and phantoms. In this paper, we describe the micro-SPECT device integrated with a new 3D optical imaging system. Simultaneously with micro-SPECT scanning, the animal is photographed with a digital camera from multiple angular positions to reconstruct a 3-dimensional optical image. We use a mathematically defined algorithm to do the optical 3D processing [8, 9].

Finally, we added x-ray CT capabilities to the system using a clinical mammography instrument (LORAD M III), a phosphor screen and a digital camera. 3D reconstruction follows suggestions of Reader et al. [10]. Figure 2 shows a photograph of the set-up.
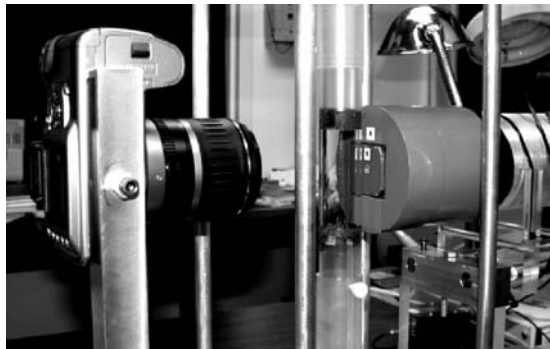

Fig. 2. Photograph of the device. Left — digital camera, middle — rotating animal holder, right – pinhole and PSPMT

Thus, the paper describes a micro-SPECT system, an Optical Imaging system (including 3D Surface Rendering and Bioluminiscence Imaging), and an x-ray CT system.

1. METHODS AND RESULTS

1.1. Coordinate Reconstruction in Micro-SPECT. We used the Hamamatsu R2486 PSPMT with preamplifiers that were developed for our small animal Southwestern Medical Center PET scanner [11, 12]. However, the front-end amplifiers

were modified to be able to integrate the long NaI(Tl) signal. A CAMAC crate containing three LeCroy 2248A ADCs (12 channels each) was used to digitize the 32 PSPMT signals (16 for X-direction, 16 for Y-direction). The integration gate width for each ADC was set to 700 ns. The 32 channels of LRS ADC 2248A were interfaced to a CAMAC Crate Controller model CC-32 (WIENER) that was connected to PC *via* PCI-bus to provide a readout rate of about 10^3 events/s.

Two additional ADC channels were used to measure the signals from the PSPMT dynode and the external calibration generator. The dynode signal spectra were used to measure the total energy deposited by the gamma ray, while the pulse generator signal was used for the correction of spectra pedestals.

To measure the $X-Y$ position of the gamma-ray interaction site, the anode wire profiles were fitted to Gaussian distributions. The width of the Gaussian (σ) was used to measure the Z position of the interaction. In the case of a blackened crystal, the diameter of a light spot on the photocathode is proportional to the distance from the point of interaction to the surface of total internal reflection, or Depth of Interaction (DOI).

The Gaussian fits of the wire profiles that give the X and Y coordinates of interaction are sensitive to the equalization of gains of all the channels. For the equalization of the gains, we used the anode wire spectra when the crystal was irradiated with a ^{57}Co source. Figure 3 shows a flood image from the ^{57}Co point source. While the shape of the distribution approximates the PSPMT's photocathode shape, distortions result in a non-uniform density.
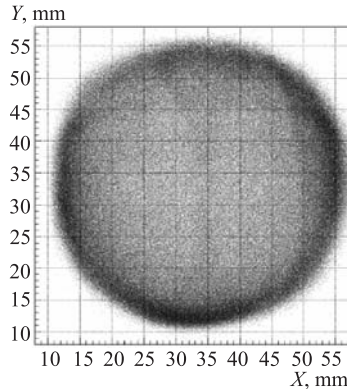

Fig. 3. A flood image from a ^{57}Co source. Despite generally correct shape of photocathode, one can see some distortions resulting in non-uniform density, besides the obvious edge effects

To control the distortion of coordinates we made an exposure of the crystal with a remote ^{57}Co source through a 2 mm thick lead mask with regularized holes of 1 mm diameter at exact 5 mm steps (Fig. 4, Left). To correct the obvious distortions, we interpolated the measured X and Y coordinates between the coordinates for the neighboring holes. The result after the corrections is presented in Fig. 4 (Right). The residual distortions are less than 0.3 mm.

To prove that the principle of DOI measurements illustrated in Fig. 1 is working, we measured correlations between the X and Y light spot sizes. If the principle is working, then the X and Y light spot sizes that are proportional to the depth of interaction in the crystal should follow each other. Of course, additional signal broadening in the dynode system of PSPMT could mask the effect. Figure 5 (left panel) presents a plot of $(\sigma_x - \sigma_y)$ *vs* $(\sigma_x^2 + \sigma_y^2)^{1/2}$ for the
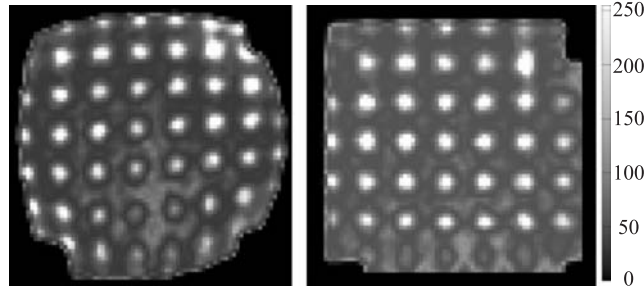
3

Fig. 4. Left — exposure of the crystal through the lead mask with regularized holes. Right — result after corrections
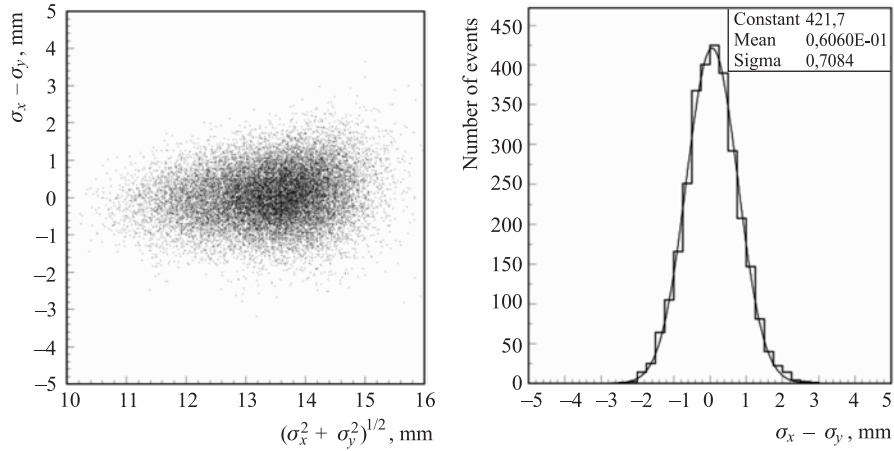

Fig. 5. Left plot presents plot $(\sigma_x - \sigma_y)$ vs $(\sigma_x^2 + \sigma_y^2)^{1/2}$ for the events from the ^{57}Co source flood exposure. Right plot shows the distribution of $(\sigma_x - \sigma_y)$ presenting the typical slice of the left plot

events from the ^{57}Co source flood exposure. It can be seen that there is a tendency of σ_x and σ_y to follow each other well as expected. Figure 5 (right panel) shows the distribution of $(\sigma_x - \sigma_y)$ presenting the typical slice of the left plot. The R.M.S. in $(\sigma_x - \sigma_y)$ is 0.7 mm. We have reasons to believe that the X and Y spot size measurements are practically independent. We could conclude then that the R.M.S. in σ_x, σ_y is about 0.5 mm, and the R.M.S. in $(\sigma_x + \sigma_y)/2$ would be about 0.35 mm. Therefore, for typical total internal reflection angles of about $45°$, accuracy in the Z direction (depth in the crystal) is given by $\sigma_z \approx 0.35$ mm. We note that such a DOI accuracy in crystals is the best reported.
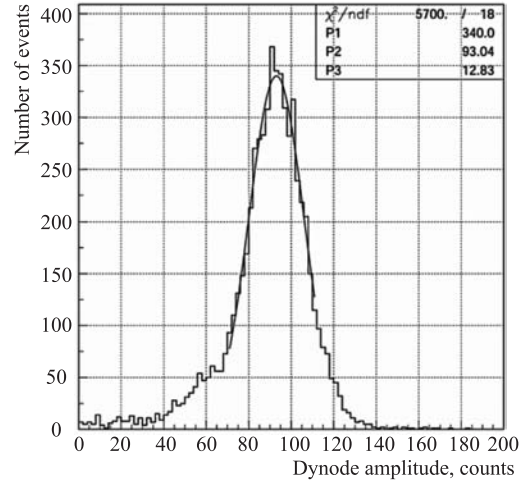
4

Fig. 6. Dynode charge amplitude spectrum (energy distribution) for the events from ^{57}Co source. The FWHM energy resolution is about 25%. Signals with low amplitudes were suppressed by the gate discriminator

Figure 6 shows the dynode amplitude spectrum (energy distribution) of the events from ^{57}Co. The FWHM energy resolution is about 25%. We expect $\Delta E/E \sim 17\%$ if retro-reflection layer on the upper surface of the crystal is used.

Summary of gamma camera characteristics is given in the Table.

Basic characteristics of the gamma camera

Active area	50 mm
Field of view	40×40 mm^2
Intrinsic spatial resolution	1 mm FWHM
NaI(Tl) scintillator dimensions	6 mm thick, 60 mm in diameter
Front shielding	Pb, 3.5 mm thick
Pinhole	Pb, diameter 0.8 mm, 90 degrees

1.2. Scan of a Mouse and Image Reconstruction. After the tests with the ^{57}Co source, we made a live scan of a normal 25 g nude male mouse after administration of 1 mCi of ^{99m}Tc methylenediphosphonate (MDP), a gamma-emitting radionuclide agent used primarily in skeletal imaging. Due to the scanner's limited field of view, the scan was performed with two translations in the vertical direction. For each translation, the same 18 evenly spaced angular positions were
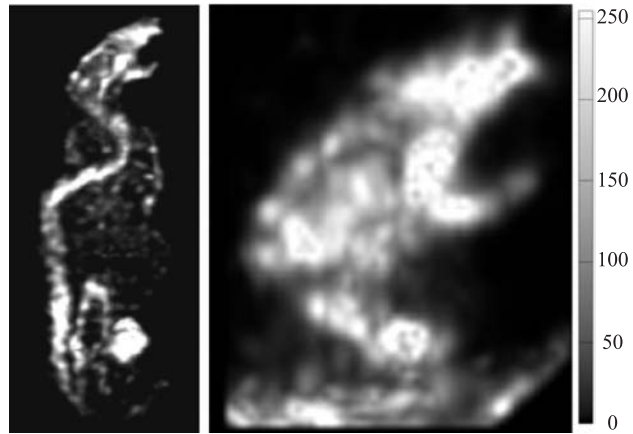
5

Fig. 7. Maximum intensity voxel projections of the mouse reconstructed image with ^{99m}Tc MDP. Left — full body of the mouse. Right — details of the head

scanned over 360 degrees. The dwell time of each projection was about one minute. The duration of the full session was about one hour, and about one million events were detected in the list mode.

We reconstructed the micro-SPECT 3D image using the Maximum Likelihood Expectation Maximization (ML-EM) algorithm of Shepp and Vardi [13] for list-
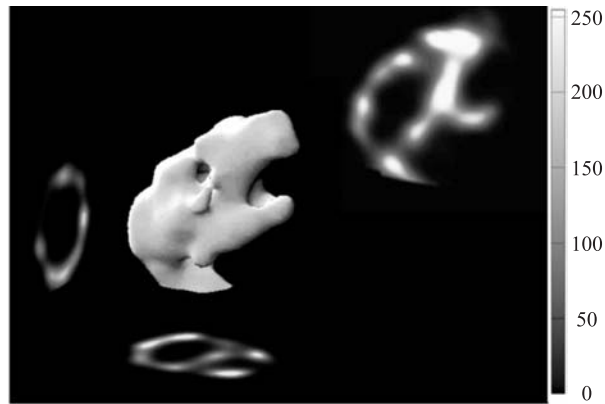

Fig. 8. Volume rendering of ^{99m}Tc MDP mouse head (center). Projections of the central slices 0.5 mm thick are also shown

6

mode data by

$$n_j^{k+1} = \frac{n_j^k}{\sum\limits_{i=1}^{I} a_{ij}} \sum_{i=1}^{M} a_{ij} \frac{1}{q_i^k} \text{ with } q_i^k = \sum_{j=1}^{J} a_{ij} n_j^k. \tag{1}$$

Here q_i^k is the expected count in line of response (LOR) i if the voxel intensity is n_i^k (at the kth iteration), a_{ij} is the probability of an emission from voxel j being detected along LOR i; M is the number of measured events and I is the number of all possible system LOR's. J is the number of voxels in the image.

Figure 7 shows Maximum Intensity Projections (MIP) of the mouse. Details of the skeletal bones of the mouse are perfectly visible. Figure 8 presents the image of volume rendering of the mouse head. Projections of the central slices of 0.5 mm thick are also shown. Typically, about 100 ML-EM iterations was necessary to get the image.

1.3. 3D Optical Imaging. Bioluminescent imaging (BLI) has already become established as a valid technique to assess gene expression in living animals and promises to offer new insight into developmental biology and gene therapy [14–17]. The technique is being widely embraced in many disciplines with recent reports relating to cardiovascular development, tumor growth and assessing diverse promoter elements [18–22]. To date, BLI has been limited to planar imaging, and commercial camera systems exist that offer high sensitivity [23]. However, planar imaging has several shortcomings [24] that limit its effectiveness as a visualization tool by hampering the precise localization of cell populations, and as a quantitative tool in estimating cell numbers (e.g., tumor burden in selected organs).

The emission nature of optical imaging looks fairly obvious. 3D optical imaging could be considered as a version of SPECT imaging, though an optical objective lens is a rather unusual collimator.

All the optical imaging cases can be broken down into three main groups. First, the case when light sources of any form are placed in a transparent medium. The second case is the imaging of reflected or diffused light from non-transparent objects. The third case, the most interesting for bioluminescent imaging, is the case when light sources are placed in a murky medium of a living tissue. We have experimented with all three types of cases.

The general method to produce a 3D image is to use a back-projection of measured intensities into a space occupied by the object. An optical objective lens is a complex optical system and the back-projection task does not appear to be straightforward, even for the simplest case (see Fig. 9). To simplify the problem, we only use the central line in Fig. 9. Thus, the optical center of the objective lens acts as a pinhole. Indeed, its position coincides with the point around which
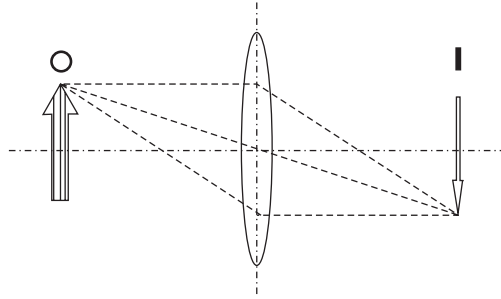
Fig. 9. Simplified schematics of optical imaging. O — the object, I — the image

the image is inverted, a point that can be experimentally determined. The back-projection line is produced when the center of a pixel at the image is connected to the optical center of the objective lens. After this procedure, the powerful methodology of medical imaging can be applied for 3D reconstruction of the image. We have adopted an approach that is closely related to 3D processing in other medical imaging modalities [8, 9]. Particularly, we used the ML-EM algorithm to reconstruct the 3D optical image. Other iterative approaches perhaps could be used as well.

Fig. 10. Experiments with optical phantom

To test our approach, we considered a simple experimental setup. Schematics explaining the experimental setup were presented in [8]. Figure 10 illustrates the experiment.

First, two red light emitting diodes (LEDs) of about 3 mm in size served as objects. Twelve angular views with a step of $30°$ were acquired by a digital camera (Sony DSC-P51) to produce a tomographic 3D image of the objects. Figure 11 shows a MIP representation of the 3D ML-EM reconstruction, the voxel size is $0.25 \times 0.25 \times 0.25$ mm^3. It can be seen that reconstruction was quite a success.

8

Fig. 11. MIP-projection of the 3D reconstruction of two light emitting diodes of 3 mm in size
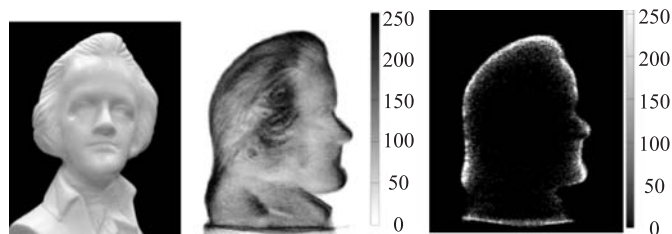

Fig. 12. 3D reconstruction of a sculptural portrait, 8 cm high. Left — the photograph, middle — the MIP image with voxel size $0.25 \times 0.25 \times 0.25$ mm^3, right — 0.5 mm central slice of the 3D image
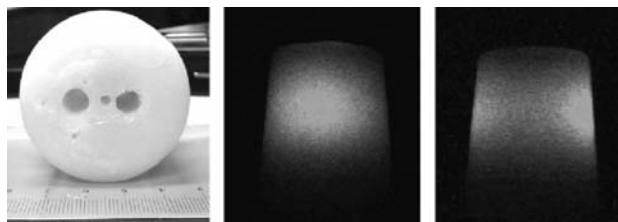

Fig. 13. The wax phantom and two photographs of LED emissions taken at orthogonal views

Second, Fig. 12 shows the 3D reconstruction of a sculptural portrait of about 8 cm high. 36 angular positions were detected with usual office luminescent lamps. Figure 12 shows that the method works fine for not only emitted, but also for reflected (diffused) light.

The third case of turbid media is the most problematic for absorption and scattering processes can distort the image. The corrections that have to be made for scattering processes in living tissue are most complicated. The main problem

9

in consistent 3D reconstruction of a light source in a tissue is the deconvolution of light scattering processes in the media. We experimented with light reconstruction in scattering media using a wax phantom and two light sources produced by LEDs. The scattering phantom was a truncated cone of wax of 55 mm in hight and about 40 mm in diameter with red light emitting diodes placed inside two holes with 15 mm center-to-center distance. Figure 13 shows the phantom and two photographs of the phantom in dark, with the LEDs on, made at orthogonal views.
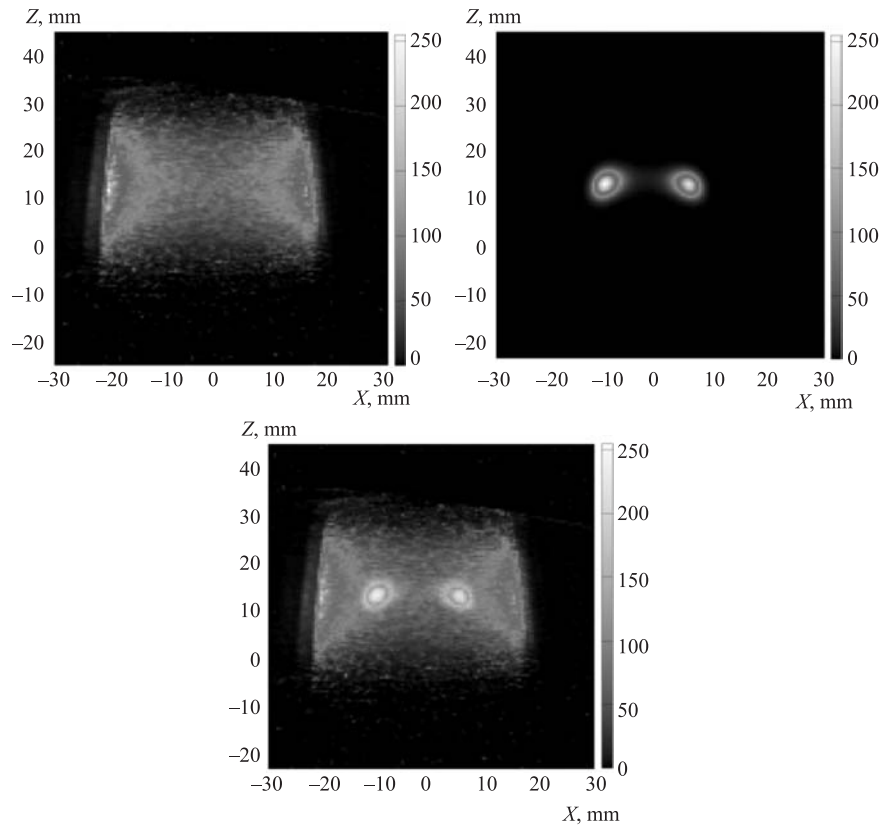

Fig. 14. Left panel — a central slice of the 3D image after ML-EM reconstruction. Right — image of the LEDs after ML-EM with deconvolution. Bottom panel – overlay of two images

ML-EM without deconvolution (i.e. system modeling) reconstructs a distribution confined essentially to the outer surface of the phantom. Figure 14 (left
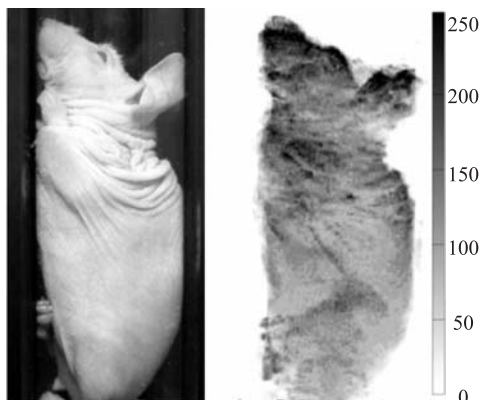
10

Fig. 15. Images of a nude mouse, left — the photograph, right — a MIP image after 3D reconstruction

panel) presents a 0.5 mm slice of the reconstructed image. Figure 14 (right) presents the results of our first attempt of deconvolving light scattering assuming a simple shift-invariant scattering kernel. This is patently a false assumption, which however, would serve to indicate further avenues for progress. The slice is again 0.5 mm thick. Figure 14 (bottom panel) is a superposition of these two images. Further computational efforts needed to make the reconstruction with a shift-variant kernel are beyond the scope of this paper.

Several experiments with optical imaging were performed using live nude mice anesthetized with isoflurane.

Figure 15 compares a photograph of a nude mouse taken in our scanner (Fig. 2) using digital camera (Canon EOS 300), and MIP image of the reconstructed 3D surface. It can be seen that a 3D image of a mouse surface could present a good complementary modality for an anatomical location of scanned organs by micro-SPECT.

Figure 16 shows the MIP projection of the sum of 3D micro-SPECT and 3D optical images of the same nude mouse in our scanner. The figure demonstrates that the co-registration of the two images is accurate.

To illustrate the power of 3D optical imaging we present Fig. 17, which is the overlay of two 3D MIP images of the nude mouse with HeLa-Luc human tumor cells in the thighs. This figure shows initial results using two HeLa-Luc tumors growing in the thighs of a nude mouse, obtained using the system described in [25] using our algorithm. For the first image, the mouse was illuminated by white light, while the second is a bioluminescence image following D-luciferin injection. The figure shows that adding a micro-SPECT to 3D optical modality would be a very powerful tool.
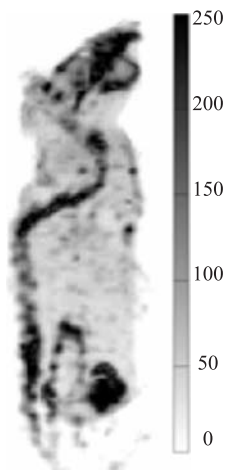
11

Fig. 16. The MIP projection of the sum of 3D micro-SPECT and 3D optical images of the same nude mouse
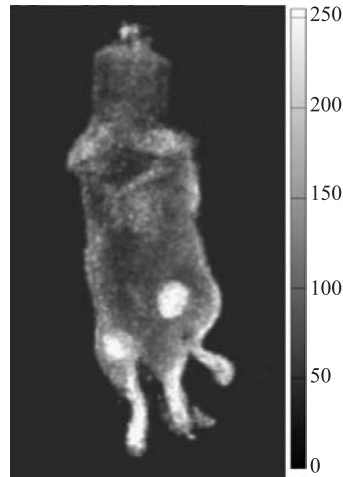

Fig. 17. Presented here is the overlay of two 3D MIP images of the nude mouse with HeLa-Luc human tumor cells in thighs, following D-luciferin injection

1.4. X-Ray CT. High efficiency in biological research studies requires that functional images obtained through metabolic markers to be co-registered with detailed anatomical images. Although the optical 3D surface of an animal can provide some topographic information, tomographic data through x-ray CT provides more detail. We have established a straight through approach for obtaining the 2D planar x-ray images that are required for CT. A schematic of the experimental setup is shown in Fig. 18.
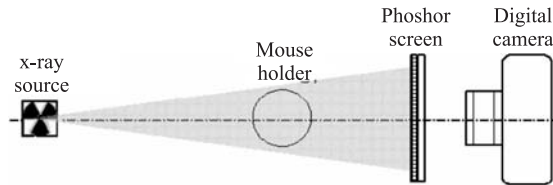

Fig. 18. Diagram of the setup for x-ray CT

The animal was irradiated using soft x-rays from a clinical mammography machine (LORAD M III) that had a Molybdenum target and 0.1 mm spot size. An insert from standard mammography film cassette (KODAK LANEX) was used as a phosphor screen. A high voltage of 30 kV and current of 17 mA was used with an exposure time of 3 s. The phosphor light was captured using a digital camera (Canon EOS 300) with an ISA of 1600 and aperture of 3.5. A dose of

12

about 10 cGy per scan is introduced. Although a more efficient phosphor screen could be used, this example demonstrates the proof of principle.

According to the ML-EM algorithm for transmission tomography projection data [10], a linear attenuation coefficient of voxel j after $k+1$ iterations is

$$\mu_j^{k+1} = \mu_j^k \frac{\sum\limits_{i=1}^{I} x_{ij} b_i \exp\left[-\sum\limits_{c=1}^{J} x_{ic}\mu_c^k\right]}{\sum\limits_{i=1}^{I} x_{ij} t_i}. \tag{2}$$

Here μ_j^k is a linear attenuation coefficient of the voxel j after k iterations; x_{ij} is an intersection length of line of response (LOR) i with voxel j; t_j is transmission projection data (a number of detected photons) for the LOR i; b_i is blank scan data (a scan taken with no attenuating object in field of view) for the LOR i; I is a number of lines of response intersecting the voxel j; and J is a number of voxels along the LOR i. Figure 19 shows two orthogonal MIP images of a nude mouse after 10 ML-EM iterations with voxel size $0.125 \times 0.125 \times 0.125$ mm^3. 36 plane images were used to reconstruct a 3D density map.
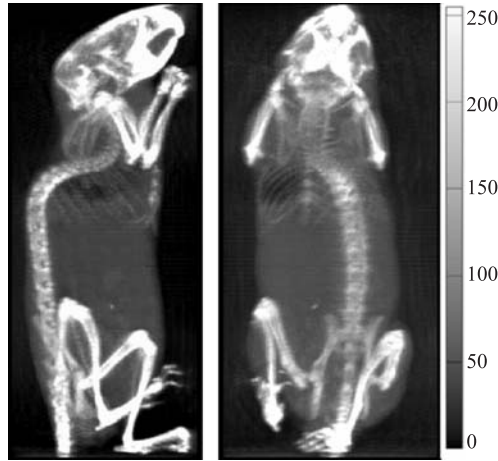

Fig. 19. Two orthogonal MIP views of CT normal mouse

2. DISCUSSION

Recently, small animal micro-SPECT has become commercially available, but is rather expensive (e.g., Gamma Medica). Here, we demonstrate a simple approach using inexpensive components, which we are using as a test bed for further developments of algorithms, detectors, and reporter agents.

13

One way to improve the spatial resolution in our micro-SPECT device is to increase the magnification scale factor. In the experiments here, we used magnification factor of about 1 to reduce the edge effects on the PSPMT. By using a Hamamatsu R3292 PSPMT, a magnification factor of 2 to 3 times is possible, with the only limiting factor of pinhole diameter remaining. The practical limit for the pinhole diameter is about 0.5 mm, dictated by overall system efficiency. A multi-pinhole system could improve system efficiency, hopefully with minor signal-to-noise degradation. When the pinhole diameter is included in 3D reconstruction with system modeling, an outstanding spatial resolution becomes possible.

The ultimate goal is correlation of several imaging modalities. Currently, commercial systems favor pairs of instruments, with insertion of an animal bed sequentially into each of the two devices, e.g., micro-SPECT and micro-CT or MRI. Optical imaging offers an alternative approach, which is directly compatible with micro-SPECT. We have demonstrated two approaches to optical imaging: firstly, 3D surface rendering (Fig. 15) plus co-registration with micro-SPECT (Fig. 16). Ultimately, full 3D optical tomography will be particularly valuable. Figure 17 shows initial results using two HeLa-Luc tumors growing in the thighs of a nude mouse, obtained using our algorithm.

The main scattering mechanism of light in tissue is refraction due to spatial variations in the refractive indexes of the tissue medium. Monte Carlo simulation of photon scattering in biological tissues has been successful. Following this direction, we intend to introduce scattering corrections into small animal optical images similar to the deconvolution approach adopted for PET scattering corrections and system modeling [12].

We have outlined a possible algorithm for 3D optical image reconstruction. While the algorithm works well in the non-scattering case, scattering corrections are expected to be large in a realistic tissue media case. Although the deconvolution mechanism for light diffusion looks straightforward, its computational effectiveness should be optimized and is a topic of separate work.

An application of Fluorescence Molecular Tomography without angular rotation was presented recently [26]. The approach is based on a method involving a normalized Born approximation with using diffusion theory through an iterative procedure. The approach looks very promising and is in line with our understanding of the deconvolution mechanism.

We should note, that our approach in optical imaging is different from popular Diffuse Optical Tomography (see, for example [27]), that could be considered as a variant of transmission imaging. In our case the optical imaging is based on the emission radiation.

Finally, in our work a simple and practical way to get tomographic images simultaneously with micro-SPECT, optical imaging and x-ray micro-CT was demonstrated.

14

CONCLUSION

Optical imaging (e.g. bioluminescence) holds great promise for increasing the available information from small animal studies. The combination of micro-SPECT imaging and 3D bioluminescence optical imaging into a single device would open new avenues in multi-modality imaging for biology and medicine. Among the disadvantages of optical imaging, was the absence of 3D image reconstruction algorithms. Accordingly, we proposed and tested a novel 3D reconstruction algorithm for optical imaging [8, 9].

In conclusion, the combination of micro-SPECT, 3D bioluminescence optical imaging and micro-CT offers a new methodology for the measurement and interpretation of biological processes. To optimize micro-SPECT detector resolution, a novel technique of 3D gamma-ray detection was incorporated in a device, and tested with a ^{57}Co source and ^{99m}Tc-MDP injected in mice. An ability of straightforward micro-CT incorporation in the system was demonstrated.

REFERENCES

1. *Del Guerra A.* Ionizing radiation detectors for medical imaging. World Scientific Pub. Co. Inc., 2004.

2. *Haberkorn U., Altmann A.* Radionuclide imaging in the post-genomic era // J. Cellular Biochemistry – Supplemen. 39, pp. 1-10, 2002.

3. *Kumar R., Jana S.* Positron emission tomography: an advanced nuclear medicine imaging technique from research to clinical practice // Meth. Enzymology. 385, pp. 3-19, 2004.

4. *Antich P., Slavin N., Tsyganov E.* PET/SPECT Detectors with Light Intensifiers and Fiber Coding // IEEE Nuclear Science Symposium & MIC-2001 Conference Record. Paper M13A-3, November 4-10, 2001, San Diego, USA.

5. *Antich P. et al.* 3D Position Readout From Thick Scintillators // Nucl. Instr. Meth. Phys. Res. A. 480/2-3, pp. 782-787. 2002.

6. *Tsyganov E. N. et al.* Micro-SPECT Using NaI(Tl) Crystals // IEEE Nuclear Science Symposium & MIC-2003 Conference Record. Paper M331, Portland, Oregon, October 19-26, 2003.

7. *Tsyganov E. N. et al.* Micro-SPECT combined with 3D optical imaging // IEEE Nuclear Science Symposium & MIC-2004 Conference Record. Paper M6-3, Rome, Italy, 16-24 October 2004.

8. *Tsyganov E. N. et al.* 3D Reconstruction Using Optical Images. arXiv.org, physics/0406148. 6 July 2004.

9. *Tsyganov E. N. et al.* Micro-SPECT combined with 3D optical imaging // IEEE Nuclear Science Symposium and Medical Imaging Conference, Rome, Italy, October 16-22, 2004, Conference Record.

10. *Reader A., Thompson C. J.* Transmission tomography algorithm for 3D list-mode and projection data // IEEE Nuclear Science Symposium and Medical Imaging Conference, (Paper M3-61), Portland, OR, October 2003.

11. *Tsyganov E. N. et al.* UT SWMC Small Animal PET Imager // IEEE Transactions on Nuclear Sciences (in press).

12. *Antich P. et al.* Application of Expectation Maximization Algorithms for Image Resolution Improvement in PET Systems // IEEE Transactions on Nuclear Science (accepted for publication).

13. *Shepp L. A., Vardi Y.* Maximum Likelihood Reconstruction for Emission Tomography // IEEE Transactions on Medical Imaging. v. MI-12, No. 2, pp. 113-121. 1982.

14. *Contag, C., Ross B.* It's not just about anatomy: in vivo bioluminescence imaging as an eyepiece into biology // J. Magn. Reson. Imaging. 16, pp. 378-387. 2002.

15. *Marx J.* Imaging. Animal models: live and in color // Science. 302 (5652) pp. 1880-1882. 2003.

16. *Herschman H. R.* Molecular imaging: looking at problems, seeing solutions // Science. 302 (5645) pp. 605-608. 2003.

17. *Marx J.* Medicine. Building better mouse models for studying cancer // Science. 299 (5615) pp.1972-1975. 2003.

18. *Hardy J. et al.* Extracellular replication of Listeria monocytogenes in the murine gall bladder // Science. 303 (5659), pp. 851-853. 2004.

19. *Vooijs M., Jonkers J., Lyons S., Berns A.* Noninvasive imaging of spontaneous retinoblastoma pathway-dependent tumors in mice // Cancer Res. 62 (6), pp. 862-867. 2002.

20. *El Hilali N. et al.* Combined noninvasive imaging and luminometric quantification of luciferase-labeled human prostate tumors and metastases // Lab. Invest. 82 (11), pp. 1563-1571. 2002.

21. *Contag C. H. et al.* Use of reporter genes for optical measurements of neoplastic disease in vivo // Neoplasia. 2 (1-2), pp. 41-52. 2000.

22. *Burgos J. S. et al.* Time course of bioluminescent signal in orthotopic and heterotopic brain tumors in nude mice // Biotechniques. 34 (6), pp. 1184-1188. 2003.

23. *Wu J. C. et al.* Molecular imaging of cardiac cell transplantation in living animals using optical bioluminescence and positron emission tomography // Circulation. 108 (11), pp. 1302-1305, Epub. 2003, Sep. 8, 2003.

24. *Paroo Z. et al.* Validating bioluminescence imaging as a high-throughput, quantitative modality for assessing tumor burden // Mol. Imaging. 3 (2), pp. 117-124. 2004.

25. *Richer E. et al.* Three-Dimensional Light Emission Tomography (LET) using Multiple Rotating CCD Cameras. Report at SMI, Saint Louis, MO, September 12, 2004.

26. *Graves E. E. et al.* A submillimeter resolution fluorescence molecular imaging system for small animal imaging // Med. Phys. 30 (5) pp. 901-911, 2003.

27. *Hielscher A. H. et al.* Near-infrared optical tomography. Desease Markers. 18, pp. 313-337, 2002.